


**Electronic states driven by the crystal field in two-dimensional materials: The case of antimonene**Tao Lei<sup>1</sup>, Jin-Mei Li<sup>2,3,\*</sup>, Shuai Lu<sup>1</sup>, Li Wang<sup>1</sup>, Qiang Yu<sup>1</sup>, Fang-Sen Li<sup>1</sup>, Jia-Ou Wang<sup>3</sup>,  
Hui-Qiong Wang<sup>4</sup>, Kurash Ibrahim<sup>2,†</sup> and Kai Zhang<sup>1,‡</sup><sup>1</sup>*Suzhou Institute of Nano-Tech and Nano-Bionics (SINANO), Chinese Academy of Sciences, Suzhou 215123, China*<sup>2</sup>*Institute of High Energy of Physics, Chinese Academy of Sciences, Beijing 100049, China*<sup>3</sup>*School of Optoelectronics, Beijing Institute of Technology, Beijing 100081, China*<sup>4</sup>*Fujian Provincial Key Laboratory of Semiconductors and Applications, Collaborative Innovation Center for Optoelectronic Semiconductors and Efficient Devices, Department of Physics, Xiamen University, Xiamen 361005, China* (Received 6 April 2021; revised 28 December 2021; accepted 24 February 2022; published 4 March 2022)

The search for novel two-dimensional (2D) giant Rashba semiconductors is a crucial step in the development of spintronic technology. The electronic properties and growth mode of antimonene grown by molecular beam epitaxy were investigated using angle-resolved photoemission spectroscopy (ARPES) and scanning tunneling microscopy. Results reveal the semiconducting nature of antimonene and the presence of a highly mobile 2D hole gas (2DHG) near the Fermi level. The anisotropy factor and Fermi velocity of the 2DHG are sensitively dependent on the crystal structure and in-plane lattice parameters of antimonene. Antimonene with small lattice parameters exhibits a small anisotropy factor and electron effective mass. Furthermore, the perpendicular (out of plane) electric field breaks the inversion symmetry and, when combined with strong spin-orbit coupling, induces the spin splitting of the valence band of antimonene. ARPES and work function measurements shed light on the band alignment between antimonene and the substrates and confirmed the presence of a nonignorable interface dipole of approximately 0.2 eV. This dipole could be the cause of approximately 80 meV spin splitting at the valence-band maximum of antimonene, a value that is significantly greater than the thermal energy at room temperature. In addition, the spin-splitting degree depends on the interface dipole strength. The gate voltage can generate the out of plane electric field and regulate the spin state similar to an internal electric field. Our results suggest that antimonene and its van der Waals heterostructure system grown on substrates could be used to develop highly efficient spin field-effect transistors and nanospintronic devices.

DOI: [10.1103/PhysRevB.105.115404](https://doi.org/10.1103/PhysRevB.105.115404)**I. INTRODUCTION**

Spintronics promises to revolutionize electronics and computing by making explicit use of the electrons' spin in addition to its charge [1]. Discovery and manipulation of new materials with large spin-orbit coupling (SOC) are crucial in the rapidly burgeoning field of spintronics [2]. The spin-orbit interaction originates from the relativistic motion of electrons and acts as an effective built-in magnetic field in nonmagnetic materials. Its function is similar to that of the external magnetic field in the celebrated quantum Hall effect [3,4]. Electrons with opposite spin states are subjected to opposite magnetic fields in their rest frame, and the field couples to their magnetic moment. Nevertheless, the net effects do not cancel out but yield a new quantum phenomenon called the Rashba effect [5], which can be manipulated by electric fields and has important applications in spintronics. In the presence of a potential gradient, SOC lifts the spin degeneracy of the band and divides the states into two bands. Their dispersions are simply approximated as  $E^\pm(k_{\parallel}) = E_0 + \frac{\hbar^2 k_{\parallel}^2}{2m^*} \pm \alpha k_{\parallel}$ , where  $m^*$  is the

effective mass, and  $\alpha$  is the Rashba coupling parameter that depends on the gradient of the potential and SOC strength [2]. States with a large Rashba spin splitting exist on the surface of several metals and in ultrathin metallic films, such as Au, Bi, Ir, and BiAg(111) alloys. The magnitudes of  $\alpha$  in Au(111) [6], Bi(111) [7], Ir(111) [8], and BiAg(111) [9] surfaces are 0.33, 0.55, 1.3, and 3.05 eV Å, respectively. Although these surface states do exhibit Rashba spin splitting, they are seldom used in spintronics devices because of difficulty in electrostatic control [10].

In addition to the strong SOC that induces a series of quantum effects, strain is an effective external method for tuning the electronic properties [11,12]. For example, the electronic structures of semiconducting transition metal dichalcogenides (TMDs) are extremely sensitive to the applied strain, thus leading to an electronic phase transition from semiconductor to metal [13]. Two-dimensional (2D) materials can accept great strain through lattice mismatch with a substrate or mechanical loading. As a 2D material with buckled structure, antimonene has a tunable in-plane lattice constant [14,15]. Uniform biaxial compressive or tensile strain can change its electronic structure, which determines its optical and electrical properties [16]. Therefore, the relationship between the strain and electronic structure of 2D materials must be established [17,18].

\*lijinmei@bit.edu.cn

†kurash@ihep.ac.cn

‡kzhang2014@sinano.ac.cn

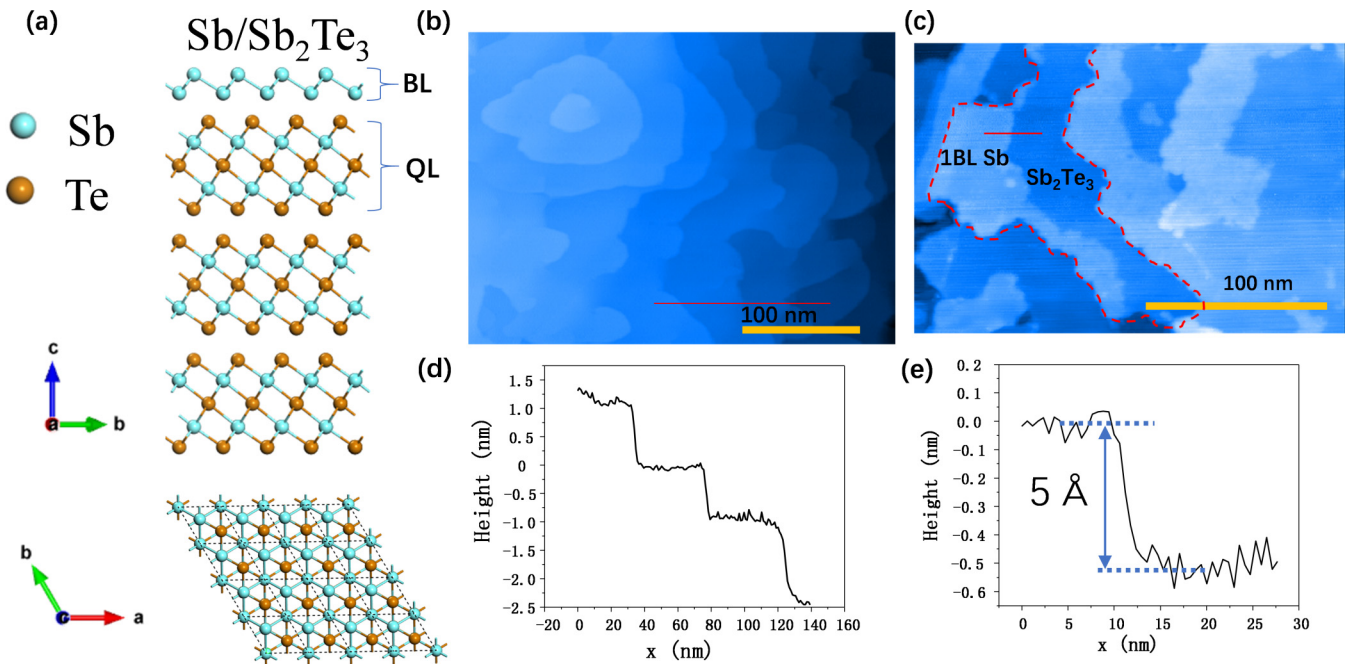


FIG. 1. (a) Perspective (left) side view and (right) top view of the atomic structure of the single Sb bilayer on the Sb<sub>2</sub>Te<sub>3</sub> surface. (b) STM image of the substrate Sb<sub>2</sub>Te<sub>3</sub> ( $V = 2.0$  V,  $I = 40$  pA). (c) STM image of the antimonene grown at approximately 0.5 BL coverage on the Sb<sub>2</sub>Te<sub>3</sub> substrate ( $V = 2.5$  V,  $I = 40$  pA). (d) Height profile taken along the red line in (b). (e) Height profile taken along the red line in (c).

Here, we report the 2D electronic systems of antimonene, a promising semiconductor material for spin field effect transistors [19,20]. Spin splitting in the valence band is revealed directly by angle-resolved photoemission spectroscopy (ARPES). The growth mode of antimonene and the physical mechanism of 2D electronic states regulated by the crystal field are systematically studied by scanning tunneling microscopy (STM), x-ray photoelectron spectroscopy (XPS), and work function measurement. The crystal field is used to summarize the periodic electric field formed by the ions of in-plane and out of plane crystals, which are affected by the in-plane lattice parameters and the broken symmetry of the out of plane crystal. A 2D hole gas (2DHG) that is sensitive to crystal symmetry and lattice parameters and has a small lattice constant, anisotropy factor, and effective mass was found in antimonene. The combination of strong SOC and out of plane asymmetrical electric field provides a spin splitting of approximately 80 meV at the valence-band maximum (VBM). Interface polarization is attributed to the change of work function and the substrate's valence band before and after the formation of a van der Waals (vdW) heterojunction. Our results show that electric fields can be used to modify the spin properties of antimonene, a candidate material with potential applications in spintronics.

## II. RESULTS AND DISCUSSION

Antimonene has a buckled honeycomb form and a hexagonal  $A7$ -type crystal structure (space group  $D_{3d}^3$ ). The crystal structure of bulk Sb is rhombohedral with two atoms in the primitive cell and can be described as a stacking of bilayers (BLs) along the [111] direction [21]. The horizontal, intra-, and inter-BL distances for bulk Sb are 4.30, 1.51, and 2.24 Å, respectively. Meanwhile, the calculated horizontal and intra-

BL lattice constants of freestanding antimonene are found to be 4.01 and 1.64 Å, respectively, which are 6.5% shorter and 7.9% longer, respectively, than the equilibrium lattice constant of bulk Sb [15,22]. This discrepancy can be attributed to the sufficient vdW forces between the Sb BLs of bulk Sb that keep the bilayer stack together, reduce the buckled strength, and flatten the horizontal lattice. When used as substrates, three-dimensional (3D) topological insulators Bi<sub>2</sub>Te<sub>3</sub> and Sb<sub>2</sub>Te<sub>3</sub> can completely satisfy the growth condition of antimonene because their crystal periodicity is only slightly mismatched with that of antimony single crystals [23]. Figure 1(a) shows the equilibrium crystal structure of antimonene/Sb<sub>2</sub>Te<sub>3</sub> heterostructure. Similar to 1 BL Bi(111) on the Bi<sub>2</sub>Te<sub>3</sub> substrate, the Sb atom is located at the hollow site of the topmost Te layers that are energetically favorable [24]. The absence of direct chemical bonding indicates that the binding is a vdW type. Figure 1(b) shows an STM image of the Sb<sub>2</sub>Te<sub>3</sub> film, and the atomically flat film provides a good template for the growth of high-quality antimonene. The STM image reveals the steps, which are quintuple layers (QLs) constituting the unit cell of Sb<sub>2</sub>Te<sub>3</sub> along the  $c$  axis, with a height of approximately 1 nm [25]. STM measurement was performed on a series of Sb films with different thicknesses deposited on Sb<sub>2</sub>Te<sub>3</sub>(111) at room temperature (RT) to investigate the nucleation and growth of antimonene. The STM image in Fig. 1(c) shows approximately 0.5 BL coverage of antimonene. The growth at RT starts from the step edge of the substrate and proceeds via a step-flow mode, indicating that the single-layer Sb film has grown layer by layer on the Sb<sub>2</sub>Te<sub>3</sub> substrate. The height profiles [Fig. 1(e)] reveal the height of Sb BL at approximately 5 Å, which matches well with that of the single Bi(111) layer grown on Bi<sub>2</sub>Se<sub>3</sub> and Bi<sub>2</sub>Te<sub>3</sub> (6 and 5 Å, respectively) [26–28]. This finding also indicates that antimonene with a

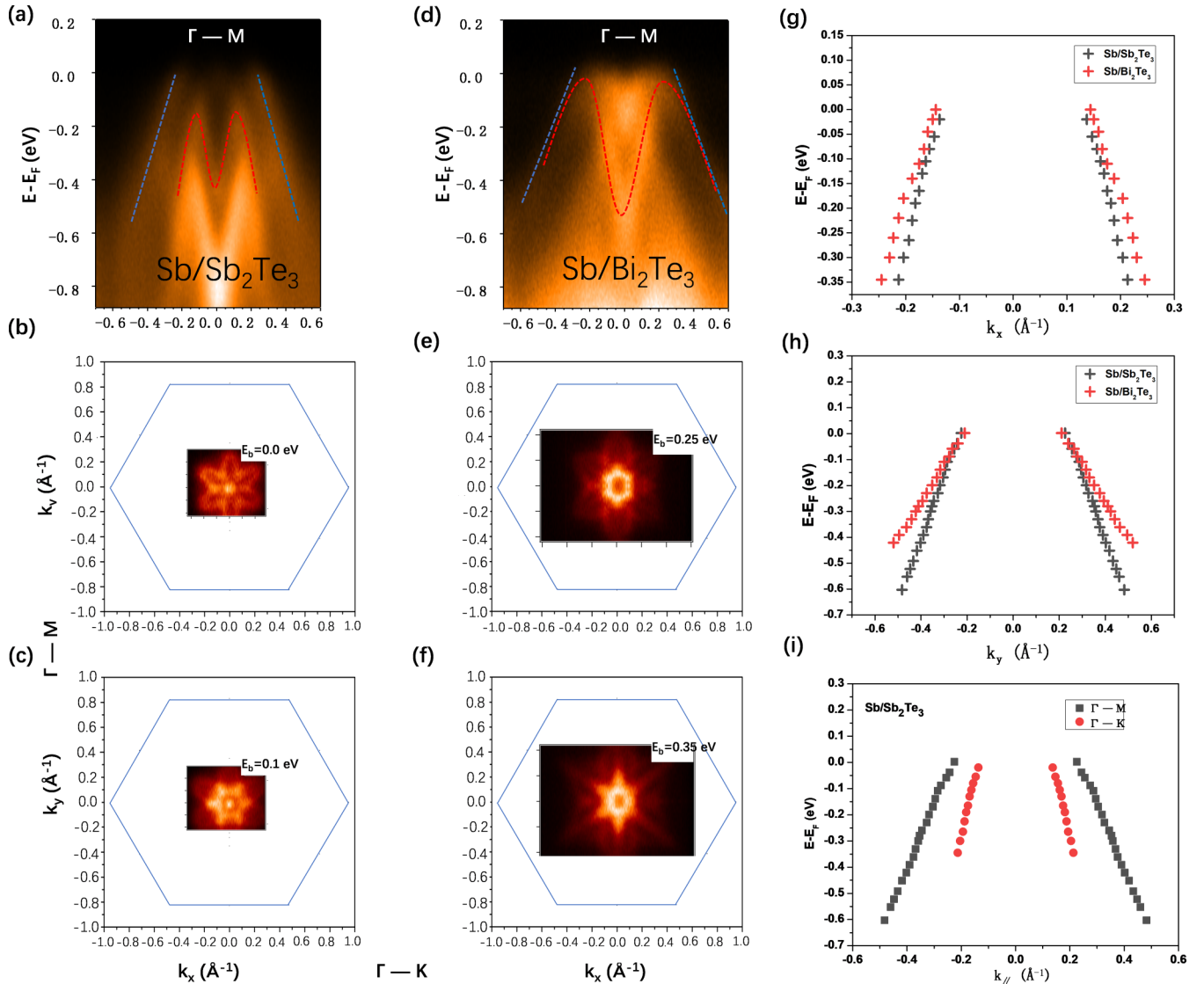


FIG. 2. ARPES measurement results of antimonene grown on substrates  $\text{Sb}_2\text{Te}_3$  (a) and  $\text{Bi}_2\text{Te}_3$  (d) along the  $\Gamma-M(k_y)$  direction. The blue and red dashed lines mark the 2DHG and valence band of antimonene, respectively. Development of the CE contour of the ARPES intensity in 2D Brillouin zone at the specified binding energies, (b), (c) for the antimonene/ $\text{Sb}_2\text{Te}_3$  system, and (e), (f) for the antimonene/ $\text{Bi}_2\text{Te}_3$  system. The contrast of 2DHG band dispersion in these two systems along the two highly symmetric directions,  $\Gamma-K(k_x)$  direction (g),  $\Gamma-M(k_y)$  direction (h). (i) Contrast of 2DHG band dispersion along the two highly symmetric directions in the antimonene/ $\text{Sb}_2\text{Te}_3$  system.

buckled structure can be grown on the  $\text{Sb}_2\text{Te}_3$  substrate with a large vdW gap between them [14].

The M-shape valence band of antimonene below the Fermi surface reveals the indirect band gap semiconductor characteristics as indicated by the red dotted lines in Figs. 2(a) and 2(d) [23]. Owing to the presence of  $\text{Sb}_2\text{Te}_3$  and  $\text{Bi}_2\text{Te}_3$ , a hole- and bulk-derived 2DHG is observed on the antimonene surface and is marked with a blue dashed line in Figs. 2(a) and 2(d). The 2DHG of antimonene on the two substrates exhibits strong anisotropy characterized by different  $k_F$  and  $v_F$  values; this quality is in contrast to the isotropy of the quasifree 2DEG on the Au(111) surface [6]. Figure 2(i) shows the band dispersion along the two highly symmetric directions  $\Gamma-K$  and  $\Gamma-M$  extracted from the ARPES measurement of the antimonene/ $\text{Sb}_2\text{Te}_3$  heterostructure. The  $k_F$  and  $v_F$  values along the  $\Gamma-K$  direction are  $0.14 \text{ \AA}^{-1}$  and  $5.4 \times 10^5 \text{ m/s}$ , re-

spectively, and those along the  $\Gamma-M$  direction are  $0.23 \text{ \AA}^{-1}$  and  $3.4 \times 10^5 \text{ m/s}$ , respectively. The corresponding anisotropy factor  $A = \frac{k^{\Gamma\mu} - k^{\Gamma\kappa}}{\langle k \rangle}$ , where  $\langle k \rangle = (k^{\Gamma\kappa} + k^{\Gamma\mu})/2$ , is measured as  $\sim 27\%$  at  $E_b = 0.3 \text{ eV}$ . As shown in Figs. 2(b), 2(c), 2(e), and 2(f), the constant energy (CE) contours of antimonene/ $\text{Sb}_2\text{Te}_3$  and antimonene/ $\text{Bi}_2\text{Te}_3$  exhibit a substantial warping effect and a hexagonal snowflake shape caused by a disorder in the in-plane crystal field [29]. In combination with the Sb ionic potential, antimonene with a hexagonal atomic structure forms a hexagonal anisotropic in-plane crystal field. The differences of the crystal potential energy lead to the differences of the band dispersion along the  $\Gamma-M$  and  $\Gamma-K$  directions, which are the origin of the materials' anisotropic properties. Comparison of the 2DHG of the antimonene/ $\text{Bi}_2\text{Te}_3$  and antimonene/ $\text{Sb}_2\text{Te}_3$  system reveals that the in-plane lattice parameters have a significant effect on the 2DHG. When a

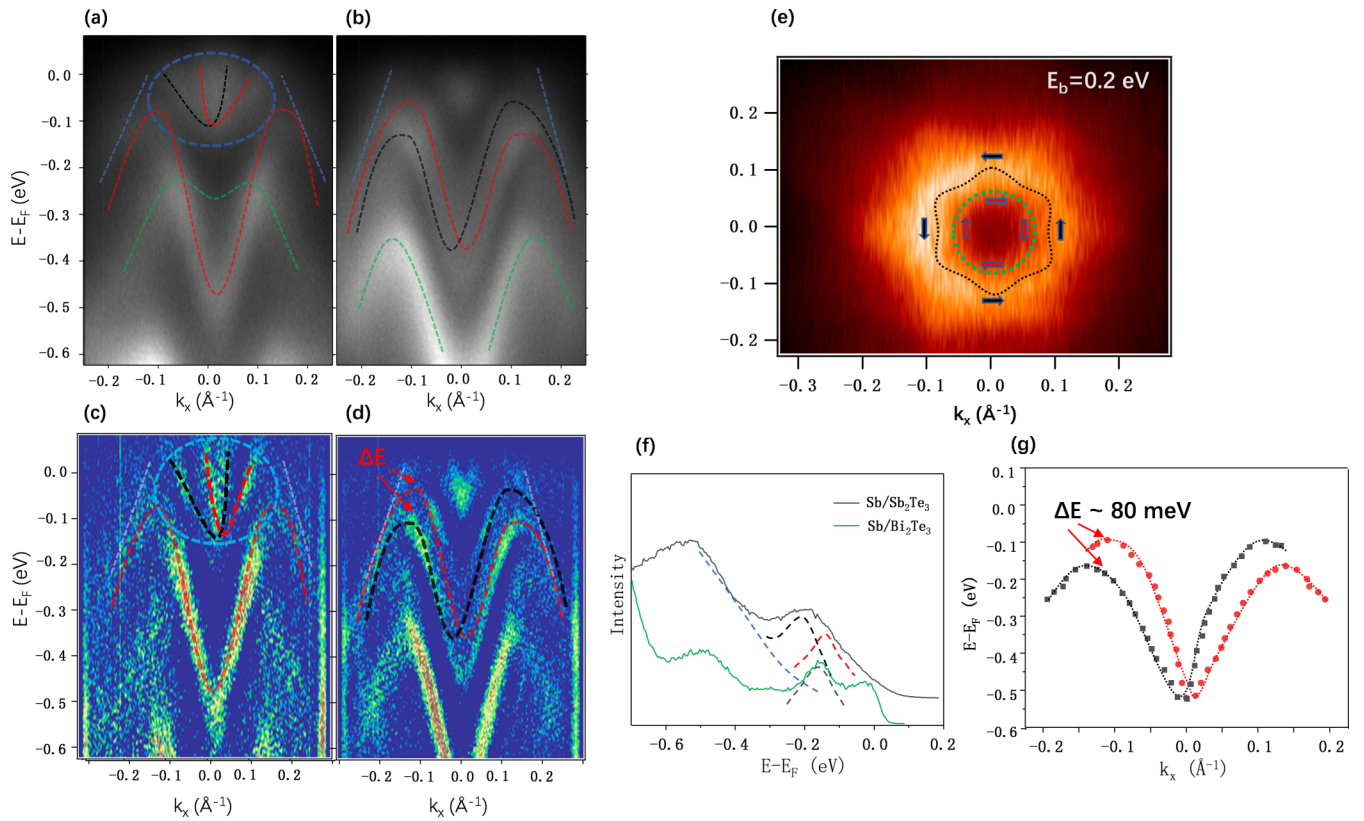


FIG. 3. Raw ARPES data of (a) antimonene/ $\text{Bi}_2\text{Te}_3$  and (b) antimonene/ $\text{Sb}_2\text{Te}_3$ . The surface states shown by the blue dotted ring indicate the presence of a slightly multilayered antimonene on  $\text{Bi}_2\text{Te}_3$ . (c), (d) are the images of the second derivative data of (a), (b), respectively. (e) Constant energy surface of antimonene/ $\text{Sb}_2\text{Te}_3$  at  $E_b = 0.2$  eV. The arrows and dashed lines represent the in-plane component of the CE surface spin texture. (f) EDCs of the two systems at  $k_x = 0.1 \text{ \AA}^{-1}$ . (g) Spin splitting of antimonene. The red and black lines represent spin-up and spin-down, respectively, and the data are extracted from (b).

low-dimensional material is grown on a suitable substrate, the atomic positions are relaxed under the constraint of the lateral lattice constants and substrate symmetry.  $\text{Sb}_2\text{Te}_3$  has the same crystal structure but smaller in-plane lattice parameters than  $\text{Bi}_2\text{Te}_3$  because the Bi atom has a larger covalent radius than the Sb atom. Figures 2(g) and 2(h) show the band dispersion along  $\Gamma$ - $K$  ( $k_x$ ) and  $\Gamma$ - $M$  ( $k_y$ ), the two highly symmetrical directions of 2DHG in these two systems. The band dispersion of 2DHG in antimonene/ $\text{Bi}_2\text{Te}_3$  with large lattice parameters is widely distributed in the momentum region, and the corresponding anisotropy factor  $A$  is approximately 59% at  $E_b = 0.3$  eV. In addition, the Fermi velocity along the  $\Gamma$ - $M$  direction in the antimonene/ $\text{Bi}_2\text{Te}_3$  system is around  $1.8 \times 10^5$  m/s, which is significantly smaller than that in the antimonene/ $\text{Sb}_2\text{Te}_3$  system with a relatively small lattice constant. The steep band dispersion in the antimonene/ $\text{Sb}_2\text{Te}_3$  system reveals its small band gap. A strong bulk conduction band near the Fermi surface is found in the antimonene/ $\text{Bi}_2\text{Te}_3$  system but not in the antimonene/ $\text{Sb}_2\text{Te}_3$  system. This finding indicates that the superior transport properties in the antimonene/ $\text{Sb}_2\text{Te}_3$  system are not affected by the substrate. According to the ARPES measurements, the band dispersion of antimonene is slightly different due to the variation in in-plane lattice constants. This result indicates that the 2DHG of antimonene is sensitively constrained by the in-plane crystal field. In particular, the 2DHG of antimonene with a small

in-plane lattice constant has weak anisotropic properties. This finding may serve as a basis for band structure modulation through interfacial stress in other 2D materials [30].

Antimonene has a strong SOC with intra-atomic spin-orbit interaction ( $\lambda = 0.34$  eV), which plays a fundamental role in the band structure [31,32]. Figure 3(b) displays the band dispersion of the antimonene/ $\text{Sb}_2\text{Te}_3$  system along the  $\Gamma$ - $K$  direction as measured by ARPES. The large spin splitting  $\Delta E$  is reflected in the topmost valence band of antimonene due to the breakage of inversion symmetry in the antimonene/ $\text{Sb}_2\text{Te}_3$  system, which is clearly resolved in the ARPES data. The second derivative data of Fig. 3(b) are presented in Fig. 3(d) to clarify the spin splitting of antimonene's valence band on the  $\text{Sb}_2\text{Te}_3$  substrate. Compared with the spin splitting of antimonene's valence band on  $\text{Sb}_2\text{Te}_3$ , that on  $\text{Bi}_2\text{Te}_3$  exhibits band features with spin degeneracy [14]. To prove that it is not a contribution from the quantum well states from the Sb films with more than a single layer, it is intentionally grown on the substrate  $\text{Bi}_2\text{Te}_3$ , and its measurement results are displayed in Figs. 3(a) and 3(c) [the second derivative data of Fig. 3(a)]. Figure 3(a) shows the band dispersion of the surface states at point  $\Gamma$ , which is characteristic of multilayer Sb films and is marked by the scope of the blue dashed line.

For additional details on this difference feature, the energy distribution curves (EDCs) at the momentum wave vector ( $k_x$ ) equal to  $-0.1 \text{ \AA}^{-1}$  are shown in Fig. 3(f). The EDCs

cross the VBM of antimonene, which is located between the binding energies of 0.1 and 0.2 eV. After background elimination, the VBM of antimonene on the  $\text{Bi}_2\text{Te}_3$  shows a single peak in a spin-degenerate state, and that of antimonene on  $\text{Sb}_2\text{Te}_3$  shows a double peak in a spin-polarized state. Figure 3(g) displays the peak positions of the EDCs corresponding to these splitting bands, and a perfect Rashba spin-splitting state is identified [33]. The spin-splitting value  $\Delta E$  of VBM in antimonene along the energy direction was adopted to quantitatively determine the strength of the Rashba spin splitting. The Rashba parameter was not selected because the Rashba energy  $E_R$  and momentum offset  $k_0$  are difficult to accurately determine due to the energy bandwidth of the valley bottom [34]. According to experimental band dispersion,  $\Delta E$  is approximately 80 meV, which is equivalent to the splitting degree in the surface state ( $\Delta E \sim 0.1$  eV) for Au(111) [6,35]. Furthermore, the large Rashba effects ensure that a well-defined spin splitting is maintained above the thermal energy at RT (26 meV at 300 K), a requirement for practical spintronics implementation. The Rashba spin splitting of the 1 BL Bi(111) surface is almost the largest among Rashba heterostructure systems [11]. However, its spin-splitting state is a surface state, which limits its applications in spintronic devices. Antimonene can overcome this limitation because the spin-splitting band coincides with its valence band. Figure 3(e) shows the spin texture of antimonene's valence band on the CE contours around point  $\Gamma$  at  $E_b = 0.2$  eV. Similar to the 2DHG of antimonene, the valence band exhibits a certain degree of warped structure due to the modulation of the hexagonal crystal field. This finding also indicates that the spin-polarization vector has components located away from the transversal direction as a consequence of the nonuniform atomic electric fields. This phenomenon is slightly different from the constant spin polarization in the concentric rings of free electrons, such as the spin structure in Au(111) [6,35].

The spin-polarized state and spin-degenerate state of antimonene deposited on  $\text{Sb}_2\text{Te}_3$  and  $\text{Bi}_2\text{Te}_3$  are found to be two different quantum states, and this finding agrees with the first principles calculation results with or without SOC [19]. Exploring the physical mechanism underlying the quantum state change of materials will aid in understanding and effectively regulating their spin and transport properties and will lay a theoretical foundation for the application of spintronic devices based on 2D materials such as antimonene. The effective mass and anisotropy of 2D materials are sensitively modulated by their in-plane lattice constant. The substrate could affect the electronic properties of antimonene by inducing strain and interfacial charge redistribution [36]. Antimonene deposited on  $\text{Sb}_2\text{Te}_3$  ( $\text{Bi}_2\text{Te}_3$ ) presents a prototypical vdW heterostructure in which the interfacial polarization could critically influence the physical properties of antimonene. The work functions before and after the growth of antimonene on the substrate were determined using the low-energy cutoff edge of the secondary electron energy distribution curve obtained from ultraviolet photoelectron spectroscopy (UPS) measurements at photon energy  $h\nu = 21.22$  eV [Fig. 4(a)]. The samples are all conductive and were grounded to ensure their consistent zero potential during ARPES measurement. The sample was connected to a constant voltage source of

$-5$  V to ensure a bias voltage of  $-5$  V (bias =  $-5$  V) between the sample and the energy analyzer. The work function (the difference between the vacuum level  $E_{\text{vac}}$  and the Fermi level  $E_F$ ) was calculated using the formula  $\phi = h\nu - \text{SECO}$ , where the secondary electron cutoff edge (SECO) is obtained from linear extrapolation [dashed lines in Fig. 4(a)] [37]. The computed values are  $\phi(\text{Sb}_2\text{Te}_3) = 4.96$  eV,  $\phi(\text{Sb}/\text{Sb}_2\text{Te}_3) = 4.73$  eV,  $\phi(\text{Bi}_2\text{Te}_3) = 4.98$  eV,  $\phi(\text{Sb}/\text{Bi}_2\text{Te}_3) = 4.89$  eV, and  $\phi(\text{bulk Sb}) = 4.45$  eV, as summarized in Fig. 4(a). According to previous studies on similar systems, the flow direction of electrons can be judged simply by using the related work function [38]. When antimonene is formed on substrates  $\text{Sb}_2\text{Te}_3$  and  $\text{Bi}_2\text{Te}_3$ , the work function decreases by 0.23 and 0.09 eV, respectively. Therefore, the change of the total work function  $\Delta\phi$  due to heterostructure formation is 0.23 eV in the antimonene/ $\text{Sb}_2\text{Te}_3$  system and  $\Delta\phi = 0.09$  eV in the antimonene/ $\text{Bi}_2\text{Te}_3$  system. These findings indicate that electrons transfer spontaneously from antimonene to the substrate due to the low work function of antimonene. As a result, antimonene gathers the positive charges, and the substrate accumulates the negative charges. This electron redistribution occurs at the interface, often leading to a periodic array of permanent and macroscopic intrinsic interface dipole ( $\Delta\phi_{\text{Dip}}$ ) [39], and is quite normal for a heterostructure with a vdW interlayer interaction. The internal electric field (“out of plane crystal field,” in comparison with the in-plane crystal field) is directed from antimonene to the substrate. This effect is described by the measured variation of the work function of the system. In addition, band bending is not observed during the ARPES measurement for the VBM of the substrate ( $\Delta V_{\text{BB}} \sim 0$  eV).  $\Delta\phi$  can be expressed as  $\Delta\phi = \Delta\phi_{\text{Dip}} + \Delta V_{\text{BB}}$  [40], and  $\Delta V_{\text{BB}}$  and  $\Delta\phi$  can be obtained from the results of ARPES and the work function. Hence, the intrinsic interface dipole  $\Delta\phi_{\text{Dip}}$  of the two systems can be calculated, and  $\Delta\phi_{\text{Dip}}$  is basically equal to  $\Delta\phi$ . Upon efficient charge transfer at the 2D-3D heterointerface in the  $\text{Sb}/\text{Sb}_2\text{Te}_3$  system, an interface electronic structure diagram can be derived by combining all the photoemission studies [Fig. 4(c)]. This interface dipole is a consequence of the interfacial electron redistribution between antimonene and the substrates and is also in agreement with other vdW heterojunction systems, such as  $\text{MoS}_2/\text{GaN}$  and  $\text{SnS}/\text{graphene}$  [41,42]. The interface dipole degree of the antimonene/ $\text{Sb}_2\text{Te}_3$  system is significantly greater than that of the antimonene/ $\text{Bi}_2\text{Te}_3$  system. The breakage of the inversion symmetry induced by the interface dipole ( $\Delta\phi_{\text{Dip}} \sim 0.23$  eV) removes the band degeneracies at the VBM ( $\Delta E \sim 80$  meV) of antimonene in the antimonene/ $\text{Sb}_2\text{Te}_3$  system. However, no significant spin splitting is observed in the antimonene/ $\text{Bi}_2\text{Te}_3$  system [Fig. 3(a)], and the three reasons are as follows: The interface dipole degree of the antimonene/ $\text{Bi}_2\text{Te}_3$  system ( $\Delta\phi_{\text{Dip}} \sim 0.09$  eV) is significantly smaller than that of the antimonene/ $\text{Sb}_2\text{Te}_3$  system ( $\Delta\phi_{\text{Dip}} \sim 0.23$  eV), and the energy resolution of the instrument based on He-I $\alpha$  is insufficient to measure the small band splitting, and at last, the natural broadening that is also present in material lead energy-band overlap. These experimental results reveal that reversible and controllable Rashba splitting and the electrostatic gating is an effective approach to tune the spin of antimonene (including spin splitting or not, and the degree of spin splitting), and the value of the interface dipole  $\Delta\phi_{\text{Dip}}$ , which also

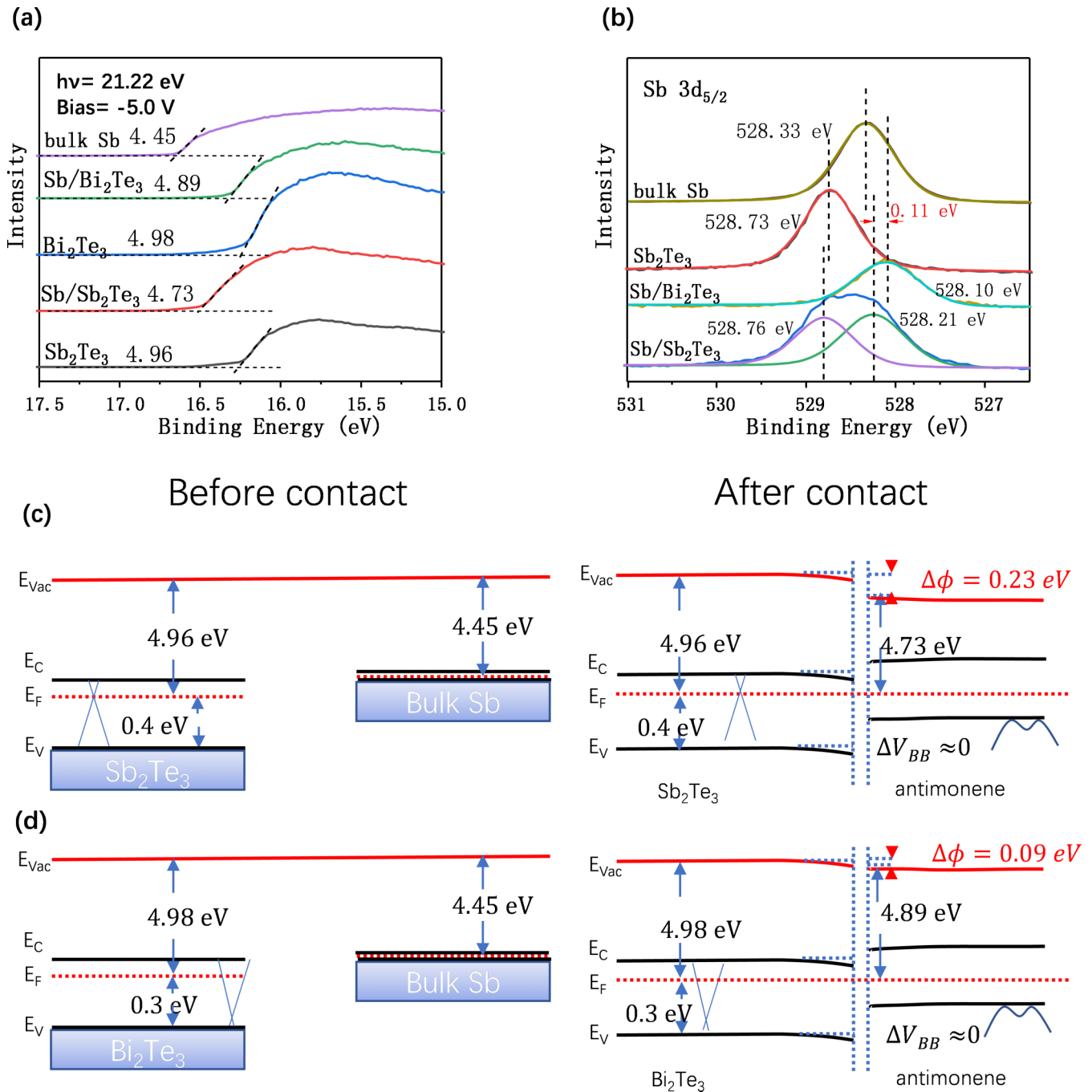


FIG. 4. (a) SECO edge was obtained for the sample by applying a bias voltage of  $-5.0$  V and He-I light of 21.22 eV. (b) Sb  $3d_{5/2}$  core-level spectra of Sb/Sb<sub>2</sub>Te<sub>3</sub>, Sb/Bi<sub>2</sub>Te<sub>3</sub>, Sb<sub>2</sub>Te<sub>3</sub>, and bulk Sb were measured at RT and taken at  $h\nu = 720$  eV. (c), (d) are the schematic of the band alignment diagram of Sb/Sb<sub>2</sub>Te<sub>3</sub> and Sb/Bi<sub>2</sub>Te<sub>3</sub> before contact (left) and after contact (right) obtained from ARPES and work function measurement.  $E_{\text{vac}}$ ,  $E_{\text{C}}$ ,  $E_{\text{F}}$ , and  $E_{\text{V}}$  are the vacuum level, conduction-band minimum, Fermi level, and valence-band maximum (VBM), respectively. The crossing lines in the band gap of substrates and M shapes were used to mark the Dirac cone and valence band of antimonene.

provides reference for the external electric field regulation. However, the specific formulation relationship between  $\Delta\phi_{\text{Dip}}$  and  $\Delta E$  may be highly sophisticated and thus need further theoretical and computational research [43].

The Coulomb interaction of the vdW heterostructure's interface can also be observed from the chemical shift of the core level [11]. This section focuses on the nature of the bonding between antimonene and the two substrates. Figure 4(b)

shows the  $3d_{5/2}$  core-level spectrum of Sb<sub>2</sub>Te<sub>3</sub>, Sb/Sb<sub>2</sub>Te<sub>3</sub>, Sb/Bi<sub>2</sub>Te<sub>3</sub>, and bulk Sb. The Sb  $3d_{5/2}$  spectra of Sb/Sb<sub>2</sub>Te<sub>3</sub> show two peaks: (1) from the Sb<sub>2</sub>Te<sub>3</sub> substrate that is not completely covered by antimonene (528.76 eV), and (2) from antimonene (528.21 eV). Peaks 1 and 2 represent the Sb-Te polar covalent bonding of the substrate and the Sb-Sb non-polar covalent bonding of antimonene, respectively. The Sb  $3d_{5/2}$  binding energy of Sb/Bi<sub>2</sub>Te<sub>3</sub> is 528.10 eV, which shifts

by 0.11 eV toward a lower binding energy compared with that in Sb/Sb<sub>2</sub>Te<sub>3</sub>. The difference in the Sb 3d<sub>5/2</sub> core levels of the two systems suggests the distinct nature of the vdW bonding; this feature is attributed to the weaker electronegativity of Bi compared to that of Sb. The Pauling electronegativity of Bi, Sb, and Te is 2.02, 2.05, and 2.10, respectively [44]. As a result, the overall electronegativity of Bi<sub>2</sub>Te<sub>3</sub> is weaker than that of Sb<sub>2</sub>Te<sub>3</sub>. With this characteristic, the bond between antimonene and Sb<sub>2</sub>Te<sub>3</sub> is strengthened, and a polar vdW interface similar to the Sb-Te polar covalent bond is formed. When band splitting  $\Delta E$  for antimonene is induced by the intrinsic interface dipole and strong SOC, an external electric field would continuously modulate the electron redistribution at the interface and eventually tune the  $\Delta E$ . Therefore, the band spin-splitting degree of antimonene can be controlled by the gate voltage, and its carrier mobility can be regulated by the lattice stress. This work paves the way for antimonene use in the development of highly efficient spin field-effect transistors and optoelectronic devices in the spintronics industry [45].

### III. CONCLUSIONS

In summary, we have provided a systematic analysis of the growth mode and the electronic properties of single-layer antimony crystals (antimonene). The 2DHG of antimonene presents anisotropic hexagonal CE contours due to the

hexagonal in-plane crystal field induced by the hexagonal crystal structure. Moreover, the anisotropy factor and Fermi velocity of antimonene are sensitively dependent on its in-plane lattice parameters. Antimonene with the small lattice parameters exhibits a small anisotropy factor and electron effective mass. The polarized out of plane crystal field drives the electronic structure of antimonene to undergo spin orbit assisted band splitting. The band diagram and interface dipole were determined by combining ARPES and work function results. The data on the physical mechanism of the obtained vdW heterostructures serve as an important basis in building electronic and spintronic devices based on antimonene. The use of substrate or gate voltage to induce and control Rashba splitting can be applied to other 2D materials with a strong SOC. The findings on electronic structures driven by the crystal field are important in understanding and controlling the physical properties of low-dimensional systems.

### ACKNOWLEDGMENTS

We thank Wei Ji and Haixia Cheng from the Renmin University of China for participating in helpful discussions. This work was supported by the National Key R&D Program of China (Grant No. 2016YFA0401002) and the National Natural Science Foundation of China (Grants No. 61875223, No. 11375228, and No. 11575227), and was funded by the China Postdoctoral Science Foundation (Grant No. 2021M701589).

- 
- [1] S. Datta and B. Das, Electronic analog of the electro-optic modulator, *Appl. Phys. Lett.* **56**, 665 (1990).
- [2] E. E. Krasovskii, Spin-orbit coupling at surfaces and 2D materials, *J. Phys.: Condens. Matter* **27**, 493001 (2015).
- [3] D. J. Thouless, M. Kohmoto, M. P. Nightingale, and M. den Nijs, Quantized Hall Conductance in a Two-Dimensional Periodic Potential, *Phys. Rev. Lett.* **49**, 405 (1982).
- [4] E. Saitoh, M. Ueda, H. Miyajima, and G. Tatara, Conversion of spin current into charge current at room temperature: Inverse spin-Hall effect, *Appl. Phys. Lett.* **88**, 182509 (2006).
- [5] E. I. Rashba, Properties of semiconductors with an extremum loop. I. Cyclotron and combinational resonance in a magnetic field perpendicular to the plane of the loop, *Sov. Phys. Solid State* **2**, 1109 (1960).
- [6] S. LaShell, B. A. McDougall, and E. Jensen, Spin Splitting of an Au(111) Surface State Band Observed with Angle Resolved Photoelectron Spectroscopy, *Phys. Rev. Lett.* **77**, 3419 (1996).
- [7] Y. M. Koroteev, G. Bihlmayer, J. E. Gayone, E. V. Chulkov, S. Blugel, P. M. Echenique, and P. Hofmann, Strong Spin-Orbit Splitting on Bi Surfaces, *Phys. Rev. Lett.* **93**, 046403 (2004).
- [8] A. Varykhalov, D. Marchenko, M. R. Scholz, E. D. L. Rienks, T. K. Kim, G. Bihlmayer, J. Sanchez-Barriga, and O. Rader, Ir(111) Surface State with Giant Rashba Splitting Persists under Graphene in Air, *Phys. Rev. Lett.* **108**, 066804 (2012).
- [9] C. R. Ast, J. Henk, A. Ernst, L. Moreschini, M. C. Falub, D. Pacile, P. Bruno, K. Kern, and M. Griioni, Giant Spin Splitting through Surface Alloying, *Phys. Rev. Lett.* **98**, 186807 (2007).
- [10] Y. H. Park, S. H. Shin, J. D. Song, J. Chang, S. H. Han, H. J. Choi, and H. C. Koo, Gate voltage control of the Rashba effect in a *p*-type GaSb quantum well and application in a complementary device, *Solid State Electron.* **82**, 34 (2013).
- [11] T. Lei, K. H. Jin, N. Zhang, J. L. Zhao, C. Liu, W. J. Li, J. O. Wang, R. Wu, H. J. Qian, F. Liu, and K. Ibrahim, Electronic structure evolution of single bilayer Bi(111) film on 3D topological insulator Bi<sub>2</sub>Se<sub>3</sub>Te<sub>3-x</sub> surfaces, *J. Phys.: Condens. Matter* **28**, 255501 (2016).
- [12] Y. Xu, B. Yan, H. J. Zhang, J. Wang, G. Xu, P. Tang, W. Duan, and S. C. Zhang, Large-Gap Quantum Spin Hall Insulators in Tin Films, *Phys. Rev. Lett.* **111**, 136804 (2013).
- [13] W. S. Yun, S. W. Han, S. C. Hong, I. G. Kim, and J. D. Lee, Thickness and strain effects on electronic structures of transition metal dichalcogenides: 2H-*M* X-2 semiconductors (*M* = Mo, W; *X* = S, Se, Te), *Phys. Rev. B* **85**, 033305 (2012).
- [14] T. Lei, C. Liu, J.-L. Zhao, J.-M. Li, Y.-P. Li, J.-O. Wang, R. Wu, H.-J. Qian, H.-Q. Wang, and K. Ibrahim, Electronic structure of antimonene grown on Sb<sub>2</sub>Te<sub>3</sub> (111) and Bi<sub>2</sub>Te<sub>3</sub> substrates, *J. Appl. Phys.* **119**, 015302 (2016).
- [15] P. Zhang, Z. Liu, W. Duan, F. Liu, and J. Wu, Topological and electronic transitions in a Sb(111) nanofilm: The interplay between quantum confinement and surface effect, *Phys. Rev. B* **85**, 201410(R) (2012).
- [16] F. Zhang, W. Li, and X. Q. Dai, Effects of interlayer coupling on the electronic structures of antimonene/graphene van der Waals heterostructures, *Superlattices Microstruct.* **100**, 826 (2016).
- [17] J.-M. Li, T. Lei, J.-O. Wang, R. Wu, H.-J. Qian, and K. Ibrahim, In-plane crystal field constrained electronic structure of stanene, *Appl. Phys. Lett.* **116**, 106101 (2020).

- [18] J. Li, T. Lei, J. Wang, R. Wu, J. Zhao, L. Zhao, Y. Guo, H. Qian, and K. Ibrahim, Anisotropic electronic structure and interfacial chemical reaction of stanene/Bi<sub>2</sub>Te<sub>3</sub>, *J. Phys. Chem. C* **124**, 4917 (2020).
- [19] A. N. Rudenko, M. I. Katsnelson, and R. Roldán, Electronic properties of single-layer antimony: Tight-binding model, spin-orbit coupling, and the strength of effective Coulomb interactions, *Phys. Rev. B* **95**, 081407(R) (2017).
- [20] G. Pizzi, M. Gibertini, E. Dib, N. Marzari, G. Iannaccone, and G. Fiori, Performance of arsenene and antimonene double-gate MOSFETs from first principles, *Nat. Commun* **7**, 12585 (2016).
- [21] Y. F. Xu, B. Peng, H. Zhang, H. Z. Shao, R. J. Zhang, and H. Y. Zhu, First-principle calculations of optical properties of mono-layer arsenene and antimonene allotropes, *Ann. Phys. (Berlin)* **529**, 1600152 (2017).
- [22] F.-C. Chuang, C.-H. Hsu, C.-Y. Chen, Z.-Q. Huang, V. Ozolins, H. Lin, and A. Bansil, Tunable topological electronic structures in Sb(111) bilayers: A first-principles study, *Appl. Phys. Lett.* **102**, 022424 (2013).
- [23] T. Lei, J.-M. Li, F.-S. Li, J.-O. Wang, K. Ibrahim, and K. Zhang, Anisotropic electronic structure of antimonene, *Appl. Phys. Lett.* **115**, 221602 (2019).
- [24] K.-H. Jin, H. W. Yeom, and S.-H. Jhi, Band structure engineering of topological insulator heterojunctions, *Phys. Rev. B* **93**, 075308 (2016).
- [25] G. Zhang, H. Qin, J. Teng, J. Guo, Q. Guo, X. Dai, Z. Fang, and K. Wu, Quintuple-layer epitaxy of thin films of topological insulator Bi<sub>2</sub>Se<sub>3</sub>, *Appl. Phys. Lett.* **95**, 053114 (2009).
- [26] M. Chen, J.-P. Peng, H.-M. Zhang, L.-L. Wang, K. He, X.-C. Ma, and Q.-K. Xue, Molecular beam epitaxy of bilayer Bi(111) films on topological insulator Bi<sub>2</sub>Te<sub>3</sub>: A scanning tunneling microscopy study, *Appl. Phys. Lett.* **101**, 081603 (2012).
- [27] A. Eich, M. Michiardi, G. Bihlmayer, X.-G. Zhu, J.-L. Mi, B. B. Iversen, R. Wiesendanger, Ph. Hofmann, A. A. Khajetoorians, and J. Wiebe, Intra- and interband electron scattering in a hybrid topological insulator: Bismuth bilayer on Bi<sub>2</sub>Se<sub>3</sub>, *Phys. Rev. B* **90**, 155414 (2014).
- [28] S. H. Kim, K.-H. Jin, J. Park, J. S. Kim, S.-H. Jhi, T.-H. Kim, and H. W. Yeom, Edge and interfacial states in a two-dimensional topological insulator: Bi(111) bilayer on Bi<sub>2</sub>Te<sub>2</sub>Se, *Phys. Rev. B* **89**, 155436 (2014).
- [29] M. Michiardi, M. Bianchi, M. Dendzik, J. A. Miwa, M. Hoesch, T. K. Kim, P. Matzen, J. Mi, M. Bremholm, and B. B. Iversen, Strongly anisotropic spin-orbit splitting in a two-dimensional electron gas, *Phys. Rev. B* **91**, 035445 (2015).
- [30] S. Singh and A. H. Romero, Giant tunable Rashba spin splitting in a two-dimensional BiSb monolayer and in BiSb/AlN heterostructures, *Phys. Rev. B* **95**, 165444 (2017).
- [31] A. V. Lugovskoi, M. I. Katsnelson, and A. N. Rudenko, Electron-phonon properties, structural stability, and superconductivity of doped antimonene, *Phys. Rev. B* **99**, 064513 (2019).
- [32] K. W. R. Manne, Atomic Spin-orbit interaction parameters from spectral data for 19 elements, *Theor. Chim. Acta* **33**, 347 (1974).
- [33] R. H. Silsbee, Spin-orbit induced coupling of charge current and spin polarization, *J. Phys.: Condens. Matter* **16**, R179 (2004).
- [34] P. D. King, R. C. Hatch, M. Bianchi, R. Ovsyannikov, C. Lupulescu, G. Landolt, B. Slomski, J. H. Dil, D. Guan, J. L. Mi *et al.*, Large Tunable Rashba Spin Splitting of a Two-Dimensional Electron Gas in Bi<sub>2</sub>Se<sub>3</sub>, *Phys. Rev. Lett.* **107**, 096802 (2011).
- [35] M. Hoesch, M. Muntwiler, V. N. Petrov, M. Hengsberger, L. Patthey, M. Shi, M. Falub, T. Greber, and J. Osterwalder, Spin structure of the Shockley surface state on Au(111), *Phys. Rev. B* **69**, 241401(R) (2004).
- [36] C. X. Xia, B. Xue, T. X. Wang, Y. T. Peng, and Y. Jia, Interlayer coupling effects on Schottky barrier in the arsenene-graphene van der Waals heterostructures, *Appl. Phys. Lett.* **107**, 193107 (2015).
- [37] W.-j. Li, P. Wang, X.-X. Wang, J.-O. Wang, R. Wu, H.-J. Qian, K. Ibrahim, H.-Y. Li, and H.-N. Li, Fullerene film on metal surface: Diffusion of metal atoms and interface model, *Appl. Phys. Lett.* **104**, 191606 (2014).
- [38] V. O. Ozelcik, Y. M. Li, W. Xiong, and F. Paesani, Modeling spontaneous charge transfer at metal/organic hybrid heterostructures, *J. Phys. Chem. C* **124**, 4802 (2020).
- [39] W. Q. Xiong, C. X. Xia, J. Du, T. X. Wang, Y. T. Peng, Z. M. Wei, and J. B. Li, Band engineering of the MoS<sub>2</sub>/stanene heterostructure: Strain and electrostatic gating, *Nanotechnology* **28**, 195702 (2017).
- [40] H. Henck, Z. Ben Aziza, O. Zill, D. Pierucci, C. H. Naylor, M. G. Silly, N. Gogneau, F. Oehler, S. Collin, J. Brault *et al.*, Interface dipole and band bending in the hybrid *p-n* heterojunction MoS<sub>2</sub>/GaN(0001), *Phys. Rev. B* **96**, 115312 (2017).
- [41] C. X. Xia, X. Y. Chen, S. Y. Wei, and Y. Jia, Laser field and electric field effects on exciton states and optical properties in zinc-blende GaN/AlGaN quantum well, *J. Appl. Phys.* **113**, 214310 (2013).
- [42] Z. Ben Aziza, H. Henck, D. Pierucci, M. G. Silly, E. Lhuillier, G. Patriarche, F. Sirotti, M. Eddrief, and A. Ouerghi, van der Waals epitaxy of GaSe/graphene heterostructure: Electronic and interfacial properties, *ACS Nano* **10**, 9679 (2016).
- [43] N. Gao, J. C. Li, and Q. Jiang, Tunable band gaps in silicene-MoS<sub>2</sub> heterobilayers, *Phys. Chem. Chem. Phys.* **16**, 11673 (2014).
- [44] L. Pauling, *The Nature of the Chemical Bond*, 3rd ed. (Cornell University Press, Ithaca, NY, 1960).
- [45] D. W. Kang, X. P. Hao, X. Z. Li, L. B. Li, and S. J. Xie, Spin polarized current through Cu-DNA modulated by a gate voltage, *Appl. Phys. Lett.* **102**, 072410 (2013).